ROYAL SOCIETY OF CHEMISTRY

PAPER

Solid oxide cells with zirconia/ceria Bi-Layer electrolytes fabricated by reduced temperature firing†

Zhan Gao,* Victor Y. Zenou,‡ David Kennouche, Laurence Marks and Scott A. Barnett

Anode-supported solid oxide cells (SOCs) with thin bi-layer $Y_{0.16}Zr_{0.92}O_{2-\delta}$ (YSZ)/$Gd_{0.1}Ce_{0.9}O_{1.95}$ (GDC) electrolytes were prepared by a reduced-temperature (1250 °C) co-firing process enabled by the addition of a Fe_2O_3 sintering aid. The Fe_2O_3 amounts in the layers affected the formation of voids at the GDC/YSZ interface; the case with 1 mol% Fe_2O_3 in the YSZ layer and 2 mol% Fe_2O_3 in the GDC layer yielded minimal interfacial voids, presumably because of optimized shrinkage matching between the electrolyte layers during co-firing. The best cells yield fuel cell power density at 0.7 V in air and humidified hydrogen of 1.74 W cm^{-2} (800 °C) and 1.0 W cm^{-2} (700 °C). Under electrolysis conditions, i.e., air and 50 vol% H_2O−50 vol% H_2, the best cell area specific resistance is 0.12 Ω cm^2 at 800 °C and 0.27 Ω cm^2 at 700 °C. This excellent cell performance was explained by a number of factors related to the reduced firing temperature: (1) low electrolyte resistance due to minimization of YSZ/GDC interdiffusion; (2) minimal zirconate phase formation between the YSZ and the $La_{0.6}Sr_{0.4}Fe_{0.8}Co_{0.2}O_3$ (LSFC) cathode because of the dense GDC barrier layer; (3) high three phase boundary density in the Ni−YSZ anode functional layer; and (4) good pore connectivity in the Ni−YSZ support. Preliminary life testing under fuel cell and electrolysis operation shows promising cell stability.

1.   Introduction

Solid oxide cells (SOCs) have important applications for energy conversion and storage,[1] but improved devices are needed to help improve commercial viability. The next-generation intermediate-temperature (≤600 °C) SOCs, which are expected to have broader commercial applications than current (750–800 °C) SOCs, thus attracted much attention during the last decade. In the evolution of SOCs to provide reduced cell resistance and to reduce operating temperature, there has been an emphasis on improved oxygen electrodes and electrolytes. Key strategies include replacing the widely-used LSM oxygen electrode with higher performance mixed conductors such as LSCF, and replacing YSZ with higher-conductivity ionic conductors such as GDC.[2] However, there are materials and processing problems associated with these materials, including mixed conductivity in GDC electrolytes[3] and reactions forming resistive phases between LSCF and YSZ during firing.[4] One important approach to overcome these difficulties is the bi-layer GDC/YSZ electrolyte; the YSZ provides an electron-blocking layer that maintains

high cell voltage while the GDC layer acts as a barrier layer to prevent LSCF–YSZ reactions. Unfortunately, YSZ and GDC interdiffuse at typical 1400 °C firing temperatures, yielding a low-conductivity mixed layer that increases electrolyte resistance.[5] One approach to avoid this is a two-step strategy where the anode and YSZ electrolyte are co-fired at 1400 °C, followed by separate ceria deposition and lower-temperature firing steps; however, this results in considerable porosity in GDC layer that allows non-negligible LSCF–zirconia reaction.[6] Alternatively, physical vapor deposition can be utilized to deposit the dense ceria layer at moderate temperatures that avoid interdiffusion,[3,7–9] but this approach may increase fabrication cost.

It was recently shown that reducing the co-firing temperature of GDC/YSZ bi-layers was a viable method for reducing interdiffusion.[10] The resulting cells had electrolyte resistance close to that expected given the GDC and YSZ thicknesses and resistivities. However, the GDC/YSZ interface width was not accurately determined, and the interface was found to have void-like defects. Furthermore, the reduction in cell polarization resistance resulting from reduced-temperature firing could not be completely explained.

Here we present a detailed study of reduced-temperature fired bi-layer electrolyte SOCs that provides a much clearer picture of the relationships between processing, microstructure, and cell performance. In particular, analytical transmission electron microscopy is used to determine the width and chemical composition of the GDC/YSZ interface. It is shown

Department of Materials Science and Engineering, Northwestern University, 2220 Campus Drive, Evanston, IL 60208, USA. E-mail: zhan.gao@northwestern.edu

‡ Current address: Nuclear Research Center-Negev, P.O. Box 9001, Beer-Sheva, Israel.

that adjusting the sintering aid content in the YSZ and GDC layers reduces the presence of interfacial void defects, resulting in lower cell resistance than in prior reports. Microstructural analysis is used to better explain the low cell resistance, and detailed electrochemical results from optimized cells including preliminary life tests are presented.

2. Experimental section

The cells fabrication process has been described in detail previously.[10] Briefly, the anode supports were prepared by mixing NiO (J. T. Baker) and YSZ (Tosoh) with 1 : 1 weight ratio along with Tapioca starch (10 wt%), poly(vinyl butyral) (Sigma-Aldrich, 0.5 wt%), and ethanol for ∼24 h. The resulting slurry was dried, sieved (#120 mesh) and uniaxially pressed into 19 mm diameter pellets. The anode support was pre-fired from 800 °C to 1100 °C for 4 h to provide mechanical strength for further processing and ensure appropriate shrinkage during cell sintering. 1–3 mol% Fe_2O_3 (>99%, Sigma-Aldrich, UK) was used as the sintering aid for the YSZ electrolyte and GDC interlayer. The NiO–YSZ (1 : 1 weight ratio), YSZ (1 mol% Fe_2O_3), and GDC (1–3 mol% Fe_2O_3) colloidal solutions were deposited onto the supports to form the anode functional layer (AFL), YSZ electrolyte and the GDC interlayer, respectively. Subsequently, the anode support/anode/electrolyte/interlayer structures were sintered at different temperatures ranging from 1250 to 1400 °C for 4 h. An LSCF–GDC (1 : 1 weight ratio) cathode functional layer (CFL) ink was screen printed onto the GDC interlayer, followed by a pure LSCF (Praxair, Washington) cathode current collector ink. The cathode layers were then fired at 1100 °C for 2 h. The cathode active area was 0.5 cm^2. The typical cell layer thicknesses were ∼700 μm for the anode support, ∼16 μm for the anode functional layer, ∼20 μm for the LSCF–GDC cathode functional layer and ∼20 μm LSCF cathode current collector. The average thickness of the YSZ layers in all cells is 9.9 ± 1.9 μm while the average thickness of GDC layer is 2.4 ± 0.24 μm, but there was considerable cell-to-cell variation.

For the fuel cell testing, a silver grid (Heraeus Inc., Pennsylvania) was screen printed onto the cathode to enhance current collection. The cell was sealed onto an alumina tubes with Ag ink (DAD-87), Shanghai Research Institute of Synthetic Resins). During fuel cell testing, the cathode was exposed to air with flow rate of 200 sccm while the anode was exposed to humidified H_2 (3 vol% H_2O) with flow rate of 100 sccm in the temperature range of 650–800 °C. H_2–H_2O–Ar mixtures with various compositions were used to vary the H_2 partial pressures. For electrolysis testing, the oxygen electrode was exposed to air with flow rate of 200 sccm, while the fuel electrode was supplied with hydrogen flowed at 100 sccm through a heated H_2O-containing bubbler that entrained known H_2O partial pressures resulting in steam contents ranging from 3 vol% to 70 vol%. After the gas composition or operating temperature was changed, cells were stabilized for at least 30 min prior to characterization. The cell current was generated by a Keithley DC power supply. Current–voltage characteristics were measured at 10 mV increments from OCV to 0 V for fuel cell testing, and from 0 V to 1.2 V at 800 °C, 1.4 V at 750 °C, 1.5 V at

700 °C and 1.7 V at 650 °C, respectively. All power density values given are at a cell voltage of 0.7 V. For each condition, four parallel cells were tested; the relative error associated with cell-to-cell variations was within ±10%.

Electrochemical impedance spectroscopy (EIS) measurements were taken on an IM6 Electrochemical Workstation (ZAHNER, Germany) under open circuit voltage state using a 20 mV AC signal in the frequency range of from 100 mHz to 100 kHz. The cell resistances were determined by fitting the EIS data using Z-View software. The microstructure and elemental diffusion of cells after testing was characterized by scanning electron microscopy (SEM, Hitachi SU8030), electron dispersive spectroscopy (EDS, Oxford X-max 80 SDD), analytical scanning transmission atomic resolution electron microscopy (JEOL JEM-ARM200CF (probe aberration corrected 200 kV STEM/TEM with a cold field emission source) and JEOL JEM-2100 FasTEM (200 kV STEM/TEM with a field emission source). Samples were infiltrated with epoxy to minimize milling artifacts from voids and differential sputtering of the LSCF-GDC layer. Samples from each fuel cell were prepared by *in situ* lift-out in a FEI Helios NanoLab 600 SEM/focused ion beam. High voltage milling (30 kV) for rough cutting and thinning was followed by low voltage milling (5 kV and 2 kV) for final thinning to minimize beam damage.

The cells after testing were also prepared for serial sectioning. Cells were fractured and infiltrated with epoxy, then polished.[11–13] Imaging was done on a Zeiss Nvision 40 dual beam FIB-SEM. Image segmentation and 3D reconstruction was done as described elsewhere.[14] Macrohomogeneous structural parameters such as volume percent, surface areas, triple phase boundary densities, and tortuosity were then extracted from the 3D data. Particle size distributions were defined using a 3D-volumetric method developed by Munch *et al.*[15]

3. Results and discussion

Section 3.1 shows the effects of firing temperature T_F on the structure, distribution of species, and electrochemical performance for a case where 1 mol% Fe_2O_3 was added to both the YSZ and GDC electrolyte layers. Section 3.2 shows the effects of varying the amounts of Fe_2O_3 in the two layers, for the case of firing at 1250 °C. Section 3.3 presents detailed electrochemical characterization of the optimized cell: fired at 1250 °C with 1 mol% Fe_2O_3 in the YSZ layer and 2 mol% Fe_2O_3 in the GDC layer.

3.1 Effect of firing temperature

3.1.1 Electrochemical characteristics. Fig. 1 presents the voltage–current characteristics, taken from cells fired at different temperatures T_F, measured at 800 °C; the same trends are observed at other measurement temperatures. The power densities increase with decreasing T_F, from 1.48 W cm^{-2} for 1250 °C firing to 0.94 W cm^{-2} for 1400 °C-firing. Cell open circuit voltages (OCVs) range from 1.03 V to 1.07 V, in the same range as cells with dense YSZ electrolytes fired at 1400 °C.[13] (These OCVs are slightly lower than the theoretical Nernst
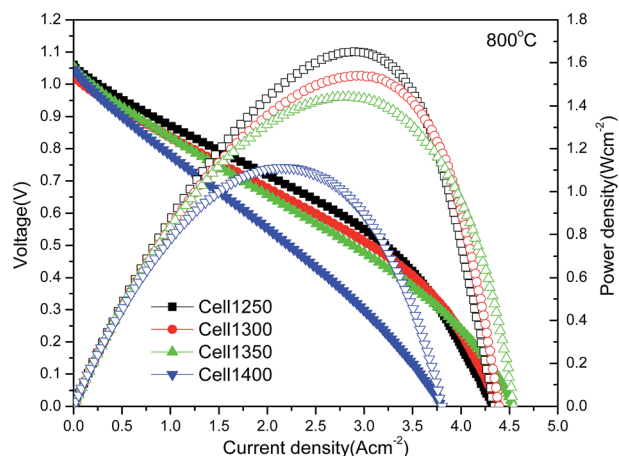
Fig. 1 Voltage and power density *versus* current density, measured at 800 °C in air and 3 vol% H_2O humidified hydrogen, for cells fired at different temperatures. 1 mol% Fe_2O_3 sintering aid was used in YSZ and GDC layers in all cases.
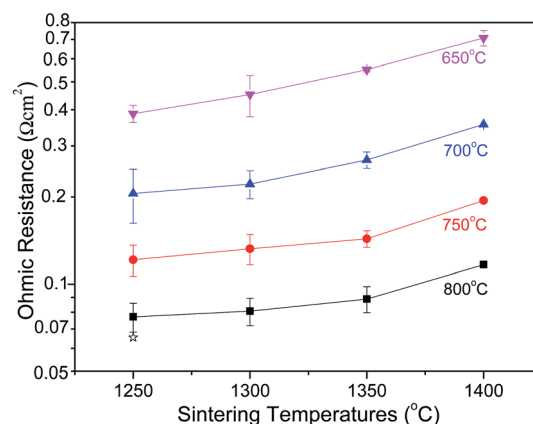

Fig. 3 Cell ohmic resistances, measured at different temperatures, *versus* firing temperature. Values from at least four different cells were averaged for each data point. The error bars represent the confidence interval at the 95% level. The star indicates the ohmic resistance for the ideal electrolyte without YSZ/GDC interdiffusion at 800 °C, estimated using literature resistivity data.

potential of 1.10 V at 800 °C with the present fuel and oxidant compositions, due to slight leakage at the Ag seals in this cell test setup.[16]) The good OCV values indicate that the electrolyte layers are reasonably dense even for $T_F = 1250$ °C and that the Fe_2O_3 addition does not introduce any electronic conduction in the electrolyte layer.

Fig. 2 presents the Bode and Nyquist plots of electrochemical impedance spectroscopy (EIS) data from the same cells shown in Fig. 1. Both the ohmic and polarization resistances decrease with the decreasing T_F, in accord with the increasing power density in Fig. 1. The spectra are modeled by three Cole–Cole elements in series with an inductor (associated with test setup wiring) and resistor (electrolyte resistance), LR(RQ)(RQ)(RQ) with $Q = Y_0(jw)^n$. The fitted curves show excellent agreement with the data. The contributions of the three impedance responses are illustrated for the case of the 1250 °C data fit. Their physical mechanisms are discussed further below.

Fig. 3 shows cell ohmic resistance values, obtained from the fits shown in Fig. 2, *versus* T_F. The ohmic resistance decreases with decreasing T_F, presumably explained by decreased YSZ–GDC interdiffusion that yields a thinner low conductivity ceria–zirconia solid solution,[17,18] consistent with prior reports.[10] The

average ohmic resistance for the four 1250 °C-fired cells was 0.075 Ω cm^2 at 800 °C, approximately that expected given the conductivities and thicknesses of the YSZ and GDC layers. That is, any contribution from an interdiffused layer was relatively small.

Fig. 2 also shows that the HF response did not change significantly with T_F, and hence this is consistent with it being from the cathode; indeed, previous measurements of LSCF–GDC symmetrical cathode cells showed a main response centered at ~1000 Hz.[19] On the other hand, the LF and MF responses decreased with decreasing T_F. Comparison with literature data for Ni–YSZ anode-supported cells[20–24] suggests that these correspond to gas diffusion concentration polarization and electrochemical hydrogen oxidation, respectively. To verify these assignments, the 1250 °C-fired cell was tested at varying temperatures and H_2 partial pressures (pH_2). As shown in Fig. 4a, the LF and MF responses increase with decreasing pH_2, providing clear evidence that these are associated with the anode. The HF response does not vary with fuel composition, again consistent with a cathode response. Fig. 5 shows the Bode (a) and Nyquist (b) plots of EIS data from the 1250 °C-fired cell measured at different temperatures. The impedance response at ~5 Hz does not vary with temperature; this, combined with
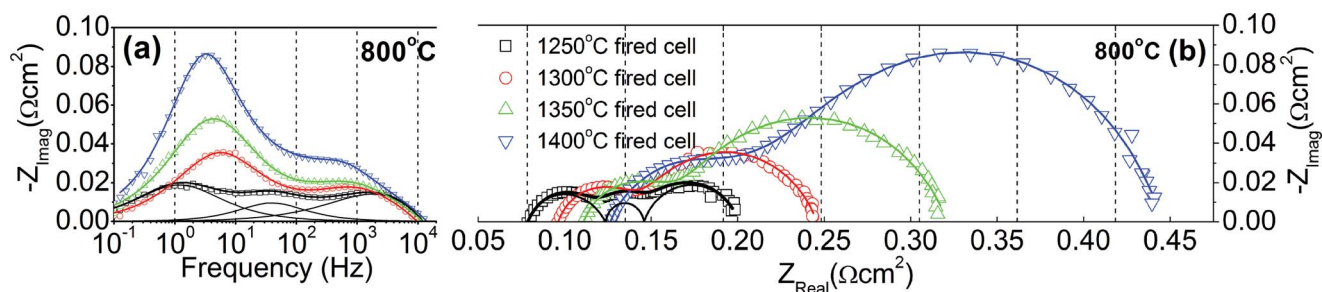

Fig. 2 Bode (a) and Nyquist (b) plots of EIS data, measured at 800 °C in air and humidified hydrogen, for cells fired at different temperatures. The curves show the fits to the data and the breakdown of the three impedance responses are shown for the case of the 1250 °C data fit.
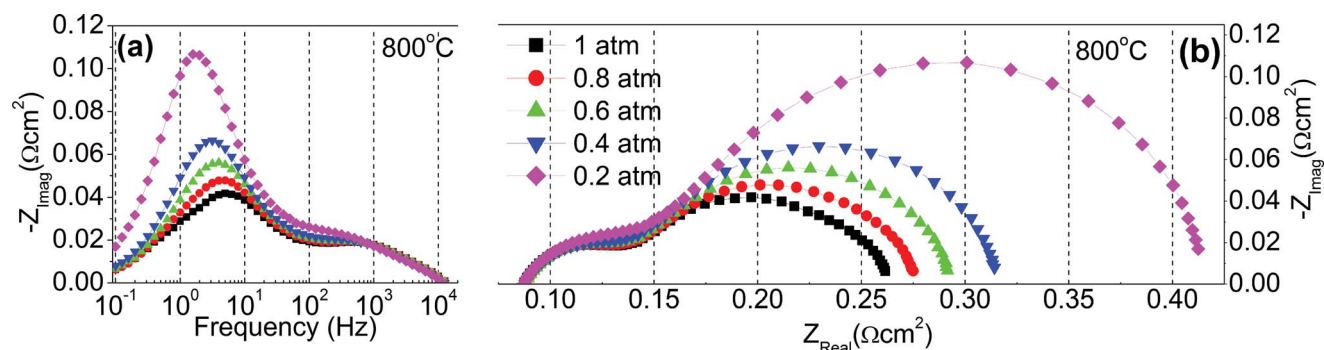
Fig. 4 Bode (a) and Nyquist (b) plots of EIS data from a 1250 °C-fired cell, measured at 800 °C in air and with different H_2 partial pressures. The H_2 was balanced by Ar while the steam partial pressure was maintained at 0.03 atm.
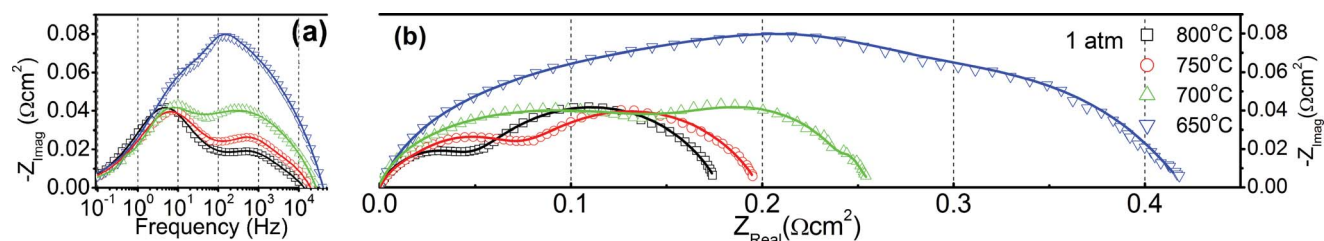

Fig. 5 Bode (a) and Nyquist (b) plots from a 1250 °C-fired cell measured at different temperatures in air and humidified hydrogen. The scattered points are the raw data; the solid lines illustrate the fitting results and the individual fitted contributions. The high-frequency intercepts of the Nyquist plots were set to zero to facilitate comparison: the high-frequency intercepts resistances are 0.087 Ω cm^2 at 800 °C, 0.136 Ω cm^2 at 750 °C, 0.224 Ω cm^2 at 700 °C and 0.397 Ω cm^2 at 650 °C.

the variation with pH_2 clearly indicates that this process is related to gas diffusion. The microstructural data presented in the following sections is used to explain the above electrochemical characteristics.

3.1.2 Electrolyte and cathode microstructure. The cells fired at 1250 °C and 1400 °C were analyzed using TEM/STEM analysis. Fig. 6 presents overview images with EDS mapping, showing Ce (red) mainly in the GDC layer, Zr (blue) mainly in the YSZ layer, and Sr (yellow) mainly in the LSCF electrode. The cathodes show the expected porous structure. The GDC and YSZ layers appear to be reasonably dense, although the 1400 °C-fired cell has a few larger isolated pores in the GDC layer, whereas the 1250 °C-fired cell shows a high density of pores at the YSZ/GDC

Fig. 6 EDS element mapping for the cells fired at 1250 °C (a) and 1400 °C (b).

interface. Although the GDC and YSZ layers appear to be almost completely separated, we believe this is an artifact of the small area measured here and perhaps of the ion thinning process – the SEM images presented below show considerable solid contact between the layers. The good density of the electrolyte layers after 1250 °C firing is probably explained by liquid phase sintering caused by the added Fe_2O_3 impurity. The rearrangement of particles and faster dissolution-transport-precipitation process in grain boundaries can be greatly facilitated by the liquid phase. Fe-rich grain boundary layers would be expected after liquid-phase sintering, but no Fe signal was detected in the EDS measurements (Fig. S1†), presumably due to the low Fe content, the low sensitivity of EDS, and the fact that the electron beam was not aligned along grain boundaries.

Fig. 6 also suggests that Zr and Ce were more interdiffused at the interface of the 1400 °C-fired cell. This was confirmed *via* STEM EDS line scans taken in the region near the YSZ/GDC interfaces (Fig. 7). The YSZ/GDC interface width, estimated as the distance between the points where the compositions reached 10% and 90% of their extreme values, decreased from ~2.5 μm at 1400 °C to ~0.5 μm at 1250 °C. Reduced interdiffusion at lower T_F is as expected. The interface width after firing at 1400 °C is in accordance with values reported previously.[5] The reduced YSZ–GDC interdiffusion in the 1250 °C-fired cell explains the decrease in electrolyte ohmic resistance with decreasing T_F, shown in Fig. 2 and 3, since the zirconia–ceria solid solution has relatively low ionic conductivity of ~1.25 × 10⁻³ S cm⁻² at 800 °C.[5] Based
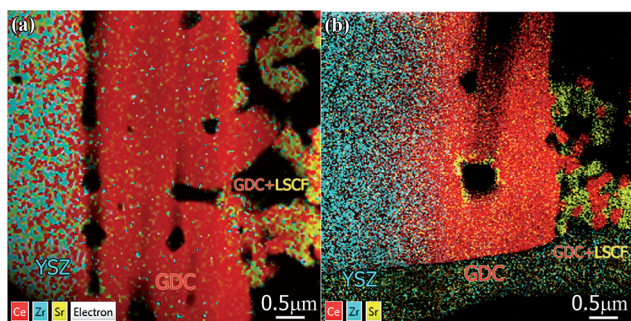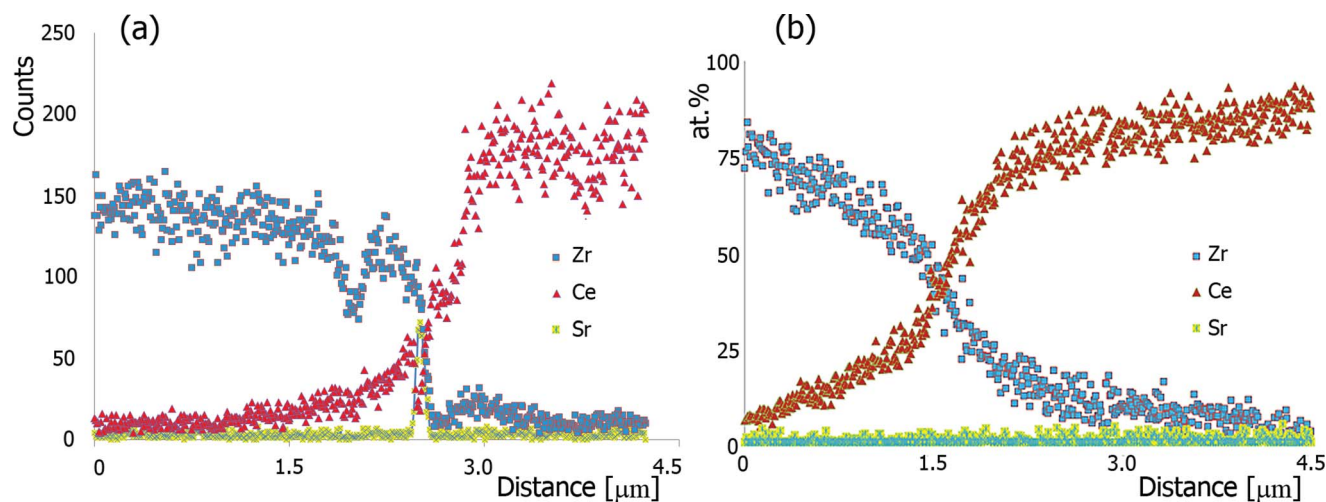
Fig. 7 EDS line scans across YSZ/GDC interface for the cells fired at 1250 °C (a) and 1400 °C (b).

on this value, the 0.5 µm interdiffusion zone for $T_F = 1250$ °C should contribute ~0.04 Ω cm², whereas the 2.5 µm interdiffusion zone for $T_F = 1400$ °C should contribute ~0.2 Ω cm². These values have the correct magnitude to explain the increase in ohmic resistance with increasing T_F in Fig. 3.

The YSZ/GDC interface of the 1250 °C-fired cell was probed chemically to check for the presence of Sr, which can diffuse from the LSCF cathode and react with YSZ to form $SrZrO_3$. Fig. 8
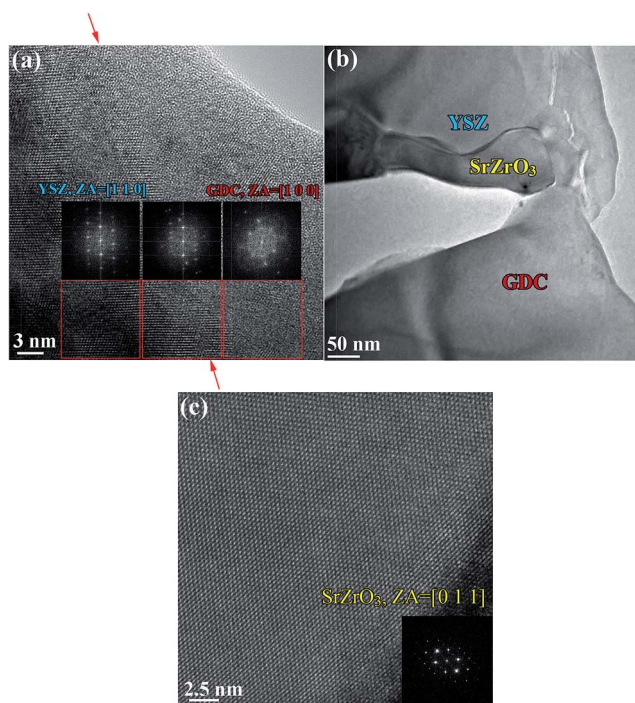

Fig. 8 (a) HREM of the regions near the YSZ/GDC interface for the cell fired at 1250 °C. The insets show Fast Fourier Transforms (FFTs) of the high resolution areas mark by red squares; (b) image showing a $SrZrO_3$ phase formed at a pore near the interface between GDC and YSZ in a cell fired at 1250 °C. (c) Lattice image and FFT showing the structure of $SrZrO_3$ along [0 1 1].

shows images of a region where there was intimate contact between YSZ and GDC (a), and a region where there was an interfacial pore (b). Fig. 8a shows a HRTEM image of the dense interface; the approximate position of the YSZ/GDC interface is marked with arrows. Fast Fourier Transform (FFT) of selected areas shows structure that fits YSZ on one side and GDC on the other side, with either zone axis ZA = [110] or ZA = [100] depending upon the local grain orientation. There is no evidence of Sr-containing phases. Fig. 8b shows a lower magnification TEM bright-field image near a pore at the YSZ/GDC interface. A Sr-rich region was detected and identified as $SrZrO_3$ in the high resolution image shown in Fig. 8c; taken along the [0 1 1] zone axis, it shows a tetragonal structure with lattice parameters $a = 5.857$ and $c = 8.301$ Å (PDF # 01-089-8999). In addition, the EDS chemical analysis shows a 1 : 1 ratio of Sr to Zr.[25] Similar results were observed for the 1400 °C-fired cell, where Sr was not detected at the YSZ/GDC interface except at voids (see Fig. 6b). These results indicate that zirconate formation only occurred at voids. While Sr diffusion was too slow through dense GDC, surface diffusion at void surfaces was fast enough to allow zirconate formation. More Sr was observed at the interface in the 1250 °C-fired cell, compared with the 1400 °C-fired cell, because of the higher density of voids.

It is shown in Section 3.2 that the interfacial voids, and hence the interfacial Sr, can be mostly eliminated by properly adjusting the sintering aid amounts. It is also shown in Section 3.2 that in 1250-fired cells, where the thin interdiffused zone contributes little excess ohmic resistance, that eliminating the interfacial voids and the associated $SrZrO_3$ reduces the electrolyte resistance significantly.

3.1.3 Anode functional layer (AFL) microstructure. The AFLs fired at different temperatures were explored by using three-dimensional tomography.[12,14] Fig. 9a and b shows 3D image representations comparing the 1250 and 1400 °C fired cells. The Ni phase feature sizes appear to be smaller for lower T_F. The results of quantitative analysis of the 3D data sets are summarized in Table 1. The mean particle sizes are 0.66 µm for Ni and 0.61 µm for YSZ in the $T_F = 1400$ °C case, and are

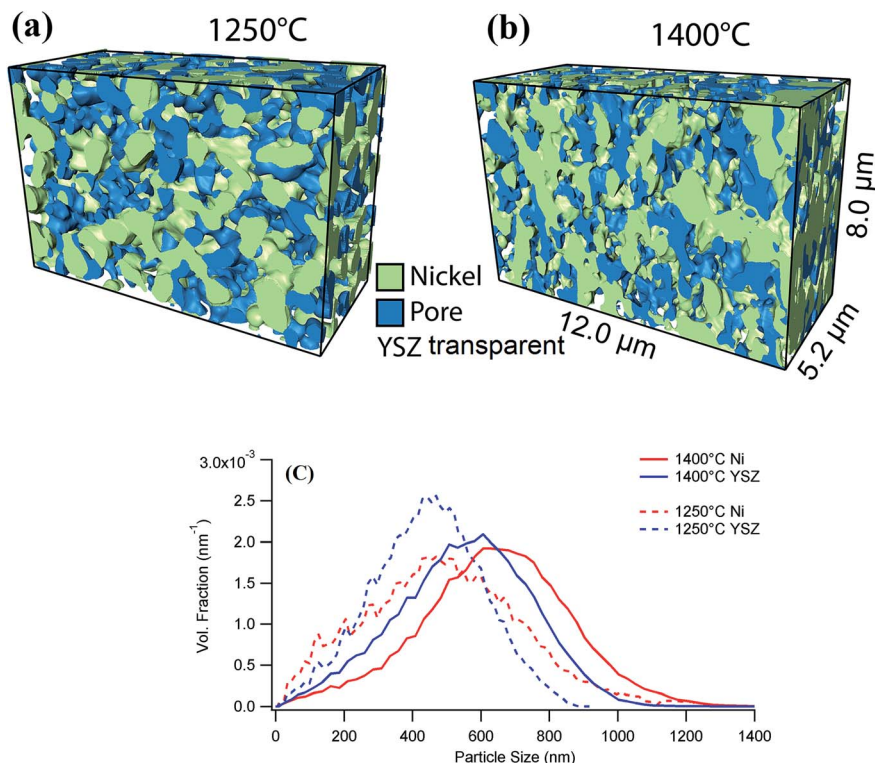**Fig. 9** 3D image reconstructions of the Ni–YSZ anodes from the cells fired at 1250 (a) and at 1400 °C (b). Ni is shown as green, pore as blue, and YSZ is transparent. (c) Normalized size distribution of the Ni and YSZ phases in different cells.

significantly smaller for the $T_F = 1250$ °C case: 0.51 μm for Ni and 0.45 μm for YSZ. These changes are also shown clearly in the feature size distributions, Fig. 9c, which also that the widths of the distributions do not change significantly. The lower particle size leads to a higher active three-phase boundary (TPB) density of 7.2 μm^{-2} for the 1250 °C-fired anode, compared to 3.0 μm^{-2} for the 1400 °C-fired cell.[26–29] The small percentage (4%) of isolated pores does not have a great impact on the active TPB density.[12,30] The pore volume fraction does not decrease significantly upon increasing the firing temperature, from 20.0 *versus* 19.2%; this indicates that the NiO–YSZ as-fired structure was nearly dense at both temperatures, with the porosity arising almost entirely from the reduction of NiO to Ni upon cell operation.[31] The pore tortuosity changes only slightly, 1.89 *versus* 1.81, so this should not influence significantly the gas diffusion concentration polarization. In any case, the AFL is quite thin compared to the anode support, and hence is expected to have little impact on concentration polarization.

3.1.4 Anode support microstructure. The substantial decrease in the EIS response at ~5 Hz in Fig. 2 suggests that decreasing T_F decreased concentration polarization, presumably in the thick anode support.[14] The large size of the pores in the Ni–YSZ anode support makes it difficult to quantitatively characterize the 3D structure using FIB-SEM, which can sample only a limited volume. Thus, 2D SEM images were taken from anode supports after reduction of the NiO to Ni. The supports were epoxy infiltrated and polished to provide clear image contrast Fig. 10 presents the segmented images for $T_F = 1300$ °C and 1400 °C. The epoxy can only infiltrate into pores that are percolated, and resulting in black contrast; on the other hand, isolated pores do not fill with epoxy and the resulting pore edges yield a white contrast in the SEM images.[14,29,32] The larger pores in the images, which resulted from the starch pore former used in the support formulation, are all black, *i.e.*, percolated. The small pores, also apparent in the images, presumably arise from a combination of incomplete sintering and the volume decrease

Table 1 Values calculated from the 3D reconstructed anode by FIB-SEM tomography

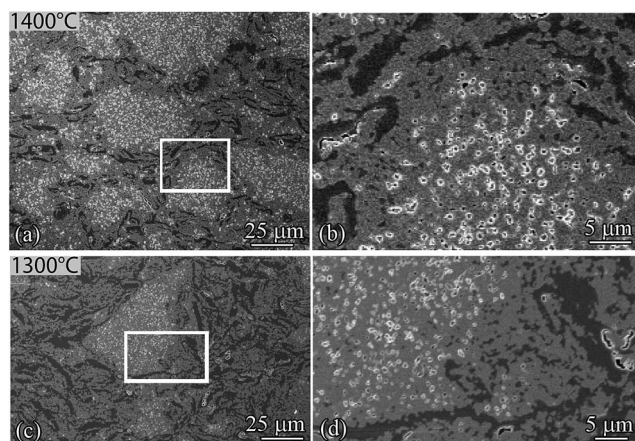|		Cell 1250	Cell 1400
Anode functional layer	Particle size of Ni (μm)	0.51	0.66
	Particle size of YSZ (μm)	0.45	0.61
	Active TPB density (μm^{-2})	7.2	3.0
	Isolated pores fraction (%)	4	4
	Pore volume fraction (%)	20.0	19.2
	Pore tortuosity	1.89	1.81

Fig. 10 SEM images of the Ni–YSZ supports for cells fired at 1400 °C (a and b) and 1300 °C (c and d). (a and c) show low magnification images. whereas (b and d) show higher magnification views of the selected areas shown as white rectangles in a and (c). In the images, the solid phases (Ni and YSZ) both have a similar medium grey contrast infiltrated pores show a dark grey contrast, and isolated pores show white around their perimeters.
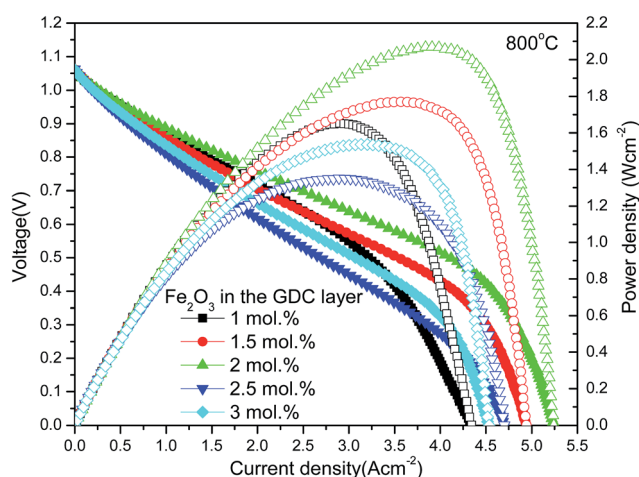

Fig. 11 Voltage and power density *versus* current density, measured at 800 °C in air and 3 vol% H_2O humidified hydrogen, for cells prepared with 1 mol% Fe_2O_3 in the YSZ layer and varying amounts (1–3 mol%) of Fe_2O_3 in the GDC layer.

upon reduction of nickel oxide to nickel. While some of these smaller pores are black (percolated), a significant fraction did not fill with epoxy as evidenced by the white contrast.

Stereological analysis was used to quantify the porosity. Comparing the two anode supports in Fig. 10, the total porosity was approximately the same for both T_F values. The large pore volume fraction is also unaffected by the sintering temperature, which seems reasonable since it resulted from a fixed amount of starch pore former and the pores were too large to sinter away. However, the lower T_F results in a larger fraction (59%) of connected small pores compared to the higher T_F (33% connected). Apparently, the reduced densification at the lower T_F substantially increases the fraction of connected pores. This should result in an associated decrease in the pore tortuosity, perhaps explaining the observed decrease in concentration polarization for reduced T_F.

3.2 Effect of sintering aid concentration

The present microstructural results and previous work[10] show a high density of voids at the YSZ/GDC interface for the 1250 °C firing temperature, even though this condition yields the best cell performance. It was hypothesized that the voids arise due to a shrinkage mismatch between the YSZ and GDC layers during firing. In this section, the effect of varying the shrinkage of the GDC layer, by varying the Fe_2O_3 sinter aid amount, was investigated for cells fired at 1250 °C. The Fe_2O_3 content in the YSZ layer was fixed at 1 mol%. Both electrochemical characteristics (Section 3.2.1) and microstructural data (Section 3.2.2) are presented.

3.2.1 Electrochemical characteristics. Fig. 11 presents the voltage–current characteristics for different cells demonstrating the effect of GDC-layer Fe_2O_3 content on the cell performance. Only the performance at 800 °C is presented since the other temperatures show the same trends. The cell with YSZ-1 mol% Fe_2O_3/GDC-2 mol% Fe_2O_3 electrolyte yields the highest power density.

Fig. 12 shows the effect of Fe_2O_3 amount on the impedance spectra taken at 800 °C on the same cells as shown in Fig. 11. The lowest Ohmic resistance is obtained for the cell with 2 mol% Fe_2O_3 in the GDC layer, which showed a measurably lower resistance of 0.058 Ω cm^2. This trend was verified by testing four different cells for each Fe content. This value is only slightly higher than the value expected given the YSZ and GDC
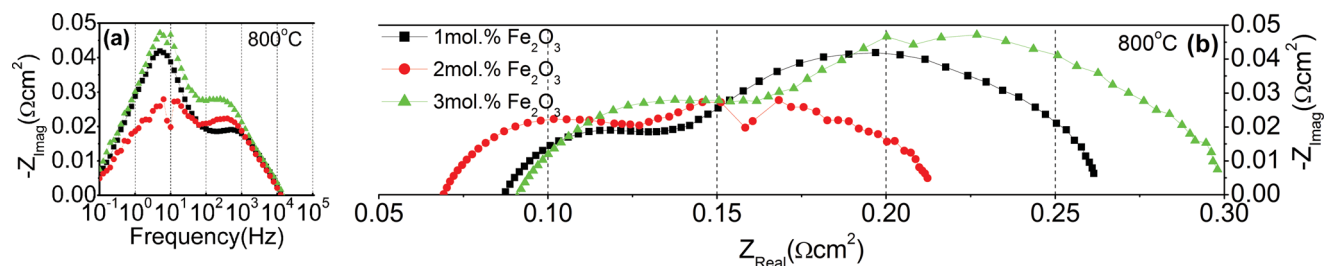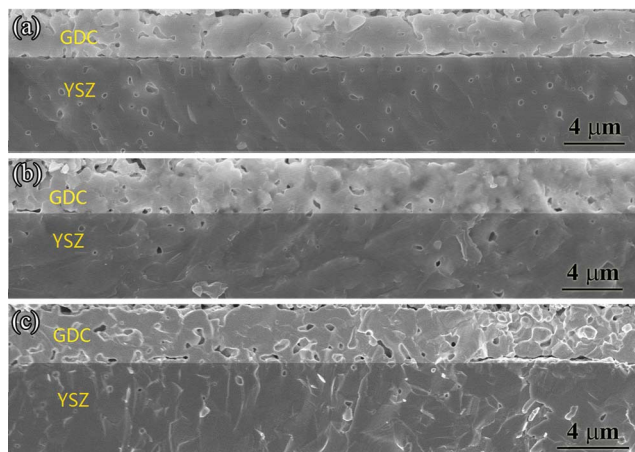

Fig. 12 Bode (a) and Nyquist (b) plots of EIS data, measured at 800 °C in air and humidified hydrogen, for cells with different Fe_2O_3 amounts in the GDC layer and 1 mol% Fe_2O_3 in the YSZ layer.

Fig. 13 Fracture cross sectional SEM images taken after testing of cells with 1 mol% Fe_2O_3 in the YSZ layers and GDC layers with 1 (a), 2 (b), or 3 (c) mol% Fe_2O_3.

layer thicknesses and their respective conductivities: at 800 °C the 9.9 µm-thick YSZ layer area-specific resistance should be 0.05 Ω cm^2 and the 2.4 µm-thick GDC layer should be 0.0043 Ω cm^2, using a conductivity value of 0.056 S cm^{-1}.[33] While the results suggest that the electrode polarization resistance was also lowest for 2 mol% Fe_2O_3, examination of many cells indicates that the changes here can be explained primarily by cell-to-cell variations, since the average polarization resistances are very close, 0.163 ± 0.024 Ω cm^2, 0.212 ± 0.052 Ω cm^2, 0.209 ± 0.032 Ω cm^2 for cells with 1 mol% Fe_2O_3, 2 mol% Fe_2O_3 and 3 mol% Fe_2O_3 addition in GDC layer respectively.

3.2.2 Cell microstructure. Fig. 13 compares fracture cross-sectional SEM images for the cells with different Fe_2O_3 content, taken after the electrochemical testing described above. The YSZ/GDC interfaces can be identified by the presence of small pores. Both the YSZ and GDC layers show reasonably dense structure. The 2 mol% Fe_2O_3 doping in GDC shows the lowest void fraction, estimated to cover ∼10% at the YSZ/GDC interface, whereas 1 mol% and 3 mol% Fe_2O_3 doping in GDC resulted in interfacial void fractions of ∼50% and ∼40%, respectively. This can perhaps be ascribed to an optimal sintering shrinkage match between the YSZ – 1 mol% Fe_2O_3 and GDC – 2 mol% Fe_2O_3. The observation that the cell Ohmic resistance was minimized for this same condition suggests that the interfacial voids, along with the associated resistive zirconate phase at the voids, do have a deleterious effect that can be eliminated by better matching layer shrinkages.

3.3 Optimized cell characteristics

Fig. 14a presents the fuel cell performance of the 1250-fired cell with optimized sintering aid concentrations measured at different temperatures. Power densities are relatively high, *e.g.*, at 0.7 V the values are 1.74 W cm^{-2} at 800 °C, 1.42 W cm^{-2} at 750 °C, and 1 W cm^{-2} at 700 °C. For comparison, the power density of similar bi-layer electrolyte cells, with dense 1 µm thick GDC layer prepared by a multiple spin-coating deposition procedure,
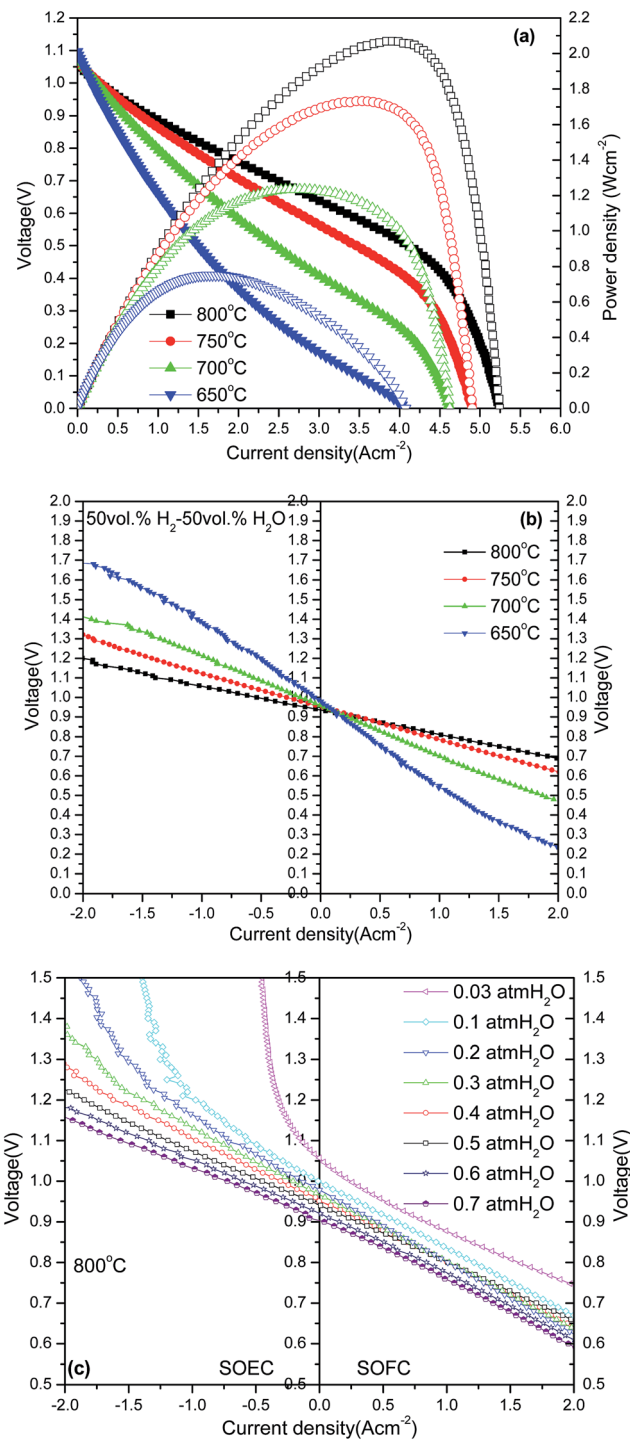

Fig. 14 (a) Voltage and power density *versus* current density, measured at different temperatures in air and humidified hydrogen. (b) Voltage *versus* current density, measured at different temperatures in air and 50 vol% H_2/50 vol% H_2O. (c) Voltage *versus* current density, measured at different temperatures in air and with different H_2O partial pressures (balance H_2). All the testing is based on an optimized cell with 1 mol% Fe_2O_3 in the YSZ layer and 2 mol% Fe_2O_3 in the GDC layer.

was 1.05 W cm^{-2} at 0.7 V at 750 °C.[34] This electrochemical performance is also much better than comparable cells with LSM cathodes.[13] Fig. S2† shows results of a preliminary >500 h

fuel cell life test at a constant current density of 1.5 A cm^{-2} at 800 °C. The cell was relatively stable, with a 10.3%/1000 h voltage degradation rate; while this value is higher than is ultimately required for SOFC stacks, it is promising for early stage cell tests.

Fig. 14b shows the voltage *versus* current density at different temperatures under electrolysis conditions, *i.e.*, with 50 vol% H$_2$/50 vol% H$_2$O on the fuel side and air on the other. The curves are fairly linear with low resistance at the higher temperatures, but show increased overpotentials and clear evidence of activated behavior at 650 °C. The total cell resistance from the slopes of the *J–V* curve is 0.12 Ω cm^2 at 800 °C and 0.27 Ω cm^2 at 700 °C; these values are somewhat lower than obtained from the fuel cell test (Fig. 14a) and the EIS data (Fig. 12) because the 50 vol% H$_2$/50 vol% H$_2$O fuel composition yields lower fuel electrode polarization than the 97 vol% H$_2$/3 vol% H$_2$O fuel used in those tests. These resistance values are quite low compared with most prior reported solid oxide electrolysis results.[35,36]

The *J–V* curves in Fig. 14a and (b) show similar characteristics, showing positive curvature at moderate current densities that becomes increasingly pronounced at lower temperature. This is consistent with the EIS data shown in Fig. 5, where activated fuel and oxygen electrode responses in the 100–1000 Hz, range both increase with decreasing temperature. A limiting current is apparent in the fuel cell data at ~5 A cm^{-2}, presumably related to the anode gas diffusion polarization seen in the EIS results (Fig. 4, 5, and 12) limiting current behavior is not seen in Fig. 14b due to the lower current densities. However, Fig. 14c, a plot of *J–V* data for the same cell at varying fuel H$_2$O contents, shows a clear decrease in the limiting current density in electrolysis mode with decreasing H$_2$O content, due to a gas diffusion limitation in the fuel electrode. Fig. S3† presents the results of a preliminary life test at 750 °C showing electrolysis voltage *versus* time under current densities of 0.5 and 0.75 A cm^{-2}. After initial degradation over the first ~50 h, the cell voltage became more stable. Approximate degradation rates were 2%/1000 h at 0.5 A cm^{-2} and 3%/1000 h at 0.75 A cm^{-2}. Increased degradation at higher current density is often observed in electrolysis operation and attributed to the oxygen electrode.[35,37]

4. Summary and conclusions

Solid oxide cells (SOCs) with bi-layer zirconia/ceria electrolytes have been successfully fabricated by low-temperature co-firing at 1250 °C and optimized by using different amounts of Fe$_2$O$_3$ sintering aid in the electrolyte layers. At 800 °C, the optimized cell yields fuel cell power density of 1.74 W cm^{-2} at 0.7 V, whereas under electrolysis conditions the cell area specific resistance is 0.12 Ω cm^2. Detailed microstructural and microchemical analysis showed that a number of factors led to the excellent cell performance: (1) low YSZ/GDC bilayer electrolyte resistance due to the mitigated interdiffusion and minimization of interfacial voids; (2) minimal Sr diffusion and SrZrO$_3$ formation between the LSFC cathode and YSZ due to the relatively dense GDC layer; (3) fine-scale Ni–YSZ anode

microstructure with high TPB density; and (4) improved anode support gas diffusion due to higher fraction of connected pores.

References

1 D. M. Bierschenk, J. R. Wilson and S. A. Barnett, *Energy Environ. Sci.*, 2011, **4**, 944–951.
2 B. C. H. Steele and A. Heinzel, *Nature*, 2001, **414**, 345–352.
3 T. P. Tsai and S. A. Barnett, *J. Electrochem. Soc.*, 1998, **145**, 1696–1701.
4 S. P. Simner, J. P. Shelton, M. D. Anderson and J. W. Stevenson, *Solid State Ionics*, 2003, **161**, 11–18.
5 A. Tsoga, A. Gupta, A. Naoumidis and P. Nikolopoulos, *Acta Mater.*, 2000, **48**, 4709–4714.
6 F. Tietz, D. Sebold, A. Brisse and J. Schefold, *J. Power Sources*, 2013, **223**, 129–135.
7 N. Jordan, W. Assenmacher, S. Uhlenbruck, V. A. C. Haanappel, H. P. Buchkremer, D. Stover and W. Mader, *Solid State Ionics*, 2008, **179**, 919–923.
8 T. Tsai and S. A. Barnett, *Solid State Ionics*, 1997, **98**, 191–196.
9 T. P. Tsai, E. Perry and S. Barnett, *J. Electrochem. Soc.*, 1997, **144**, L130–L132.
10 Z. Gao, D. Kennouche and S. Barnett, *J. Power Sources*, 2014, **260**, 259–263.
11 J. S. Cronin, K. Muangnapoh, Z. Patterson, K. J. Yakal-Kremski, V. P. Dravid and S. A. Barnett, *J. Electrochem. Soc.*, 2012, **159**, B385–B393.
12 J. S. Cronin, J. R. Wilson and S. A. Barnett, *J. Power Sources*, 2011, **196**, 2640–2643.
13 J. S. Cronin, Y. C. K. Chen-Wiegart, J. Wang and S. A. Barnett, *J. Power Sources*, 2013, **233**, 174–179.
14 D. Kennouche, Y. C. K. Chen-Wiegart, J. S. Cronin, J. Wang and S. A. Barnett, *J. Electrochem. Soc.*, 2013, **160**, F1293–F1304.
15 B. Munch and L. Holzer, *J. Am. Ceram. Soc.*, 2008, **91**, 4059–4067.

16 D. M. Bierschenk, M. R. Pillai, Y. Lin and S. A. Barnett, *Fuel Cells*, 2010, **10**, 1129–1134.

17 A. Tsoga, A. Naoumidis and D. Stover, *Solid State Ionics*, 2000, **135**, 403–409.

18 X. D. Zhou, B. Scarfino and H. U. Anderson, *Solid State Ionics*, 2004, **175**, 19–22.

19 D. M. Bierschenk, J. M. Haag, K. R. Poeppelmeier and S. A. Barnett, *J. Electrochem. Soc.*, 2013, **160**, F90–F93.

20 R. Barfod, A. Hagen, S. Ramousse, P. V. Hendriksen and M. Mogensen, *Fuel Cells*, 2006, **6**, 141–145.

21 S. H. Jensen, A. Hauch, P. V. Hendriksen, M. Mogensen, N. Bonanos and T. Jacobsen, *J. Electrochem. Soc.*, 2007, **154**, B1325–B1330.

22 A. Leonide, V. Sonn, A. Weber and E. Ivers-Tiffee, *J. Electrochem. Soc.*, 2008, **155**, B36–B41.

23 S. Primdahl and M. Mogensen, *J. Electrochem. Soc.*, 1999, **146**, 2827–2833.

24 H. Y. Zhu, A. Kromp, A. Leonide, E. Ivers-Tiffee, O. Deutschmann and R. J. Kee, *J. Electrochem. Soc.*, 2012, **159**, F255–F266.

25 S. Uhlenbruck, T. Moskalewicz, N. Jordan, H. J. Penkalla and H. P. Buchkremer, *Solid State Ionics*, 2009, **180**, 418–423.

26 J. H. Lee, H. Moon, H. W. Lee, J. Kim, J. D. Kim and K. H. Yoon, *Solid State Ionics*, 2002, **148**, 15–26.

27 K. R. Lee, S. H. Choi, J. Kim, H. W. Lee and J. H. Lee, *J. Power Sources*, 2005, **140**, 226–234.

28 Y. Nishida and S. Itoh, *Electrochim. Acta*, 2011, **56**, 2792–2800.

29 D. Kennouche, J. Hong, H.-S. Noh, J.-W. Son and S. A. Barnett, *Phys. Chem. Chem. Phys.*, 2014, **16**, 15249–15255.

30 J. R. Wilson, J. S. Cronin and S. A. Barnett, *Scr. Mater.*, 2011, **65**, 67–72.

31 J. R. Wilson and S. A. Barnett, *Electrochem. Solid-State Lett.*, 2008, **11**, B181–B185.

32 J. R. Wilson, W. Kobsiriphat, R. Mendoza, H. Y. Chen, J. M. Hiller, D. J. Miller, K. Thornton, P. W. Voorhees, S. B. Adler and S. A. Barnett, *Nat. Mater.*, 2006, **5**, 541–544.

33 V. V. Kharton, F. M. Figueiredo, L. Navarro, E. N. Naumovich, A. V. Kovalevsky, A. A. Yaremchenko, A. P. Viskup, A. Carneiro, F. M. B. Marques and J. R. Frade, *J. Mater. Sci.*, 2001, **36**, 1105–1117.

34 P. Plonczak, M. Joost, J. Hjelm, M. Sogaard, M. Lundberg and P. V. Hendriksen, *J. Power Sources*, 2011, **196**, 1156–1162.

35 R. Knibbe, M. L. Traulsen, A. Hauch, S. D. Ebbesen and M. Mogensen, *J. Electrochem. Soc.*, 2010, **157**, B1209–B1217.

36 M. B. Choi, B. Singh, E. D. Wachsman and S. J. Song, *J. Power Sources*, 2013, **239**, 361–373.

37 G. A. Hughes, K. Yakal-Kremski and S. A. Barnett, *Phys. Chem. Chem. Phys.*, 2013, **15**, 17257–17262.